Journal of Atmospheric and Solar–Terrestrial Physics 260 (2024) 106254

Contents lists available at ScienceDirect

Journal of Atmospheric and Solar–Terrestrial Physics

journal homepage: www.elsevier.com/locate/jastp

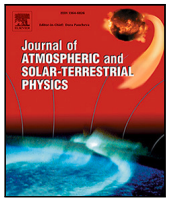

Research paper

Joule Heating rate at high-latitudes by Swarm and ground-based observations compared to MHD simulations

Kirsti Kauristie [a,*], Octav Marghitu [b], Max van de Kamp [a], Theresa Hoppe [a], Ilja Honkonen [a], Adrian Blagau [b], Ionut Madalin Ivan [b], Mihail Codrescu [c], Aaron Ridley [d], Gábor Tóth [d], Yasunobu Ogawa [e], Lorenzo Trenchi [f]

[a] Finnish Meteorological Institute, Erik Palmenin aukio 1, Helsinki, P.O. Box 503, 00101, Finland
[b] Institute for Space Sciences, Atomistilor Str. 409, Bucharest Magurele, RO-77125, Romania
[c] Space Weather Prediction Center, NOAA, W/NP9, 325 Broadway, Boulder, 80305, CO, United States
[d] University of Michigan, 2455 Hayward Street, Ann Arbor, 48109-2143, MI, United States
[e] National Institute of Polar Research, 10-3 Midori-cho, Tachikawa-shi, Tokyo, 190-8518, Japan
[f] Serco for ESA, European Space Agency, ESRIN, Largo G. Galilei 1, Frascati, Italy

ARTICLE INFO

Keywords:
Auroras
Joule heating
Magneto-Hydro-Dynamic simulations

ABSTRACT

We compare Joule Heating rates as derived from ground-based magnetic field and all-sky camera data, from Low Earth Orbit satellite data (ESA Swarm) and from a MHD simulation (GUMICS-5) with each other in a case study of an auroral arc system. The observational estimates of Joule Heating rates provide information on regional scales and with high spatial resolution (10–100 km). Their comparison with global MHD results is conducted for a quiet time interval of a few minutes, just before a magnetic substorm. Analysis of the ground-based observations yields electric field with dominating North-South component pointing towards the arcs and having maxima values in the range 20–35 V/km. Combining these values with Pedersen conductance estimates from optical data (5–10 S) yields Joule Heating rates in the range 2.5–3.5 mW/m^2. Swarm electric field measurements are consistent in their direction and intensity with the ground-based estimates. They also show that heating is increased particularly in the region where the conductance is low. The total amount of Joule heating in the area between the Swarm A and C satellite footprints while crossing the all-sky camera field of view is estimated to be 46 MW and the total amount energy dissipation during the 80 s overflight is around 3.6 GJ (1000 kWh). GUMICS-5 estimate of the peak Joule Heating in the magnetic local time sector of the arc system is smaller than that from the ground-based data with a factor of 2.9. Comparisons of GUMICS-5 results with Space Weather Modeling Framework (SWMF), shows that the latter gives on average larger heating rates being thus more consistent with our regional observations. However, both MHD-codes yield smaller Joule Heating rates around the time of the arcs and during the following substorm than the CTIP-e code. CTIP-e has a more detailed description of ionosphere-thermosphere interactions than the MHD-codes and its convection electric field is enhanced with a randomly varying additional component mimicking small scale structures. GUMICS-SWMF comparisons of global Joule Heating patterns in the Northern polar area reveal that the two simulations have significant differences in their spatial distribution of heating rates. Main cause for these deviations is the difference in the derivation of ionospheric Pedersen conductance. Our results emphasize the fact that future estimates of the global energetics in the magnetosphere–ionosphere–thermosphere system require better knowledge on ionospheric conductivities, both by new measurement concepts and by better understanding on the background physics controlling conductivity variations.

1. Introduction

Ionospheric Joule Heating (JH) is one of the main dissipation channels of the energy that solar wind feeds into the magnetosphere–ionosphere system during auroral substorms (Tanskanen, 2002). In the ionosphere JH is one element in the energy exchange between electromagnetic fields and plasma. It mainly describes that portion of energy flux which contributes to the thermal heating of the ion-neutral gas in the upper atmosphere (Aikio et al., 2012; Richmond,

* Corresponding author.
E-mail address: kirsti.kauristie@fmi.fi (K. Kauristie).

https://doi.org/10.1016/j.jastp.2024.106254
Received 11 September 2023; Received in revised form 3 May 2024; Accepted 9 May 2024
Available online 11 May 2024

2021). Estimating JH rates (JH per unit of area, $Q_E = \Sigma_p E^2$, where Σ_p is the ionospheric Pedersen conductance and **E** is the electric field) particularly on regional and global scales is challenging. In accurate assessments the JH rates should be calculated using electric field in the frame of neutral gas velocity (**u**). As observations of **u** are only sporadically available, it is often neglected and the electric field in Q_E assessments is measured or modeled in the frame of the Earth's surface. According to Aikio et al. (2012) this can lead to relative uncertainties of 20%–30% in the JH rate estimates.

Q_E has been investigated extensively with data by Incoherent Scatter Radars (ISR). ISR measurements allow deducing all the necessary parameters for careful JH assessments, not just as altitude integrated investigations, but also for information on the altitude variations in the key parameters. For Q_E – which in this paper is defined to be the altitude integrated JH rate – height profiles of electron density derived from the ISR measurement at the radar beam location, combined with empirical modeling on plasma-neutral atmosphere collision rates are used to estimate Σ_p, and ion velocity data are used to deduce **E**. This approach has been adopted e.g. in the studies of Aikio and Selkälä (2009) and Cai et al. (2016) who have used the EISCAT mainland and Svalbard radars to derive statistics on Q_E values at auroral oval latitudes and at the high-latitude afternoon hot-spot. Kavanagh et al. (2022) report similar MLT distributions of Q_E as Aikio and Selkälä (2009) and Cai et al. (2016) but they also point out that calculations of Joule heating from the ISR tristatic method can yield significantly greater values than from the monostatic depending on magnetic local time and geomagnetic activity. JH rate altitude variations including those due to variations in **u** have been studied e.g. by Aikio et al. (2012) and Zhan et al. (2021). Although altitude variations in the energy transfer between ionosphere and thermosphere is recognized as one of the main open topics in geospace research (Sarris et al., 2020), in this paper we discuss mostly altitude integrated JH with the focus on its estimates on local, regional, and global scales. This perspective is suitable for remote ionospheric observations, like those provided by the Swarm mission, performed a few 100 km above the E-layer ionospheric region, where most of the JH occurs.

In a steady state situation and when **u** is neglected, the energy source by electromagnetic field, characterized by the divergence of Poynting flux ($\mathbf{E} \times \mathbf{B}/\mu_0$), can be used as a proxy for the JH rate. That relation has been utilized by Olsson et al. (2004) who have composed a Magnetic Latitude-Magnetic Local Time (MLAT-MLT) map of average Q_E based on Low Earth Orbit (LEO) satellite electric and magnetic field recordings. The additional benefit from LEO data when compared with ISR comes from their wider latitude coverage. While the statistics of Olsson et al. (2004) are based on individual JH rate estimates along satellite tracks, Weimer (2005) has first derived statistical models for the electric and magnetic potentials from satellite data and used those potentials to compose maps of JH rates for different solar wind conditions. When interpreting Poynting flux-based JH results, it is good to recognize that Poynting flux measurements at satellite orbit do not always have pointwise correspondence with the ionospheric JH rates at the satellite foot point. The Poynting flux approach has some shortcomings particularly during active periods, when strong gradients in the ionospheric Hall and Pedersen conductances appear and consequently the Pedersen currents may also have divergence free components (Vanhamäki et al., 2012).

Based on the finding of good correlation between global JH and the Polar cap index (PC; Troshichev et al., 1988) by Chun et al. (1999), Chun et al. (2002) have derived empirical models of Q_E northern hemispheric patterns with the technique of Assimilative Mapping of Ionospheric Electrodynamics (AMIE; Richmond, 1992). As its first step AMIE modifies statistical models of ionospheric height-integrated conductance and auroral precipitation with all available observations related to these parameters. After that the conductance pattern is applied to the inversion of ground magnetic perturbations to deduce the electric potential distribution and finally to create a global view of the high-latitude electrodynamics including JH. The resulting Q_E distributions as binned according to increasing PC show distinct patterns for negative and positive PC values, where the former correspond to the situation of lobe reconnection and Q_E enhancement at dayside high-latitudes and the latter correspond to more active times and increased heating at auroral oval latitudes.

Global instantaneous pictures on high-latitude Q_E can be achieved also by MHD simulations. The event study by Palmroth et al. (2005) compares global high-latitude JH values from combined satellite and ground-based data and from geomagnetic based proxies with results from the GUMICS-4 MHD simulation (Janhunen et al., 2012). The different observational approaches give mutually rather similar results on the general time evolution of JH during the substorm event. However, there are significant differences in the actual JH values (spatially integrated Q_E) with a factor of 4 between them. Differences appear also in the spatial distributions of Q_E. Simulated JH and Q_E are smaller than the observed-based values by a factor of 10. Also Rastätter et al. (2016) report about big variability in the JH estimates as derived from the data of the Geospace Environment Modeling-Coupling Energetics and Dynamics of Atmospheric Regions modeling (GEM-CEDAR) challenge addressing six magnetic storm events of different intensities. Rastätter et al. (2016) compare Poynting flux measurements by the Defense Meteorological Satellite Program (DMSP) with empirical Poynting flux models and with JH by physics-based ionospheric models and by ionospheric electrodynamics solvers of magnetosphere MHD simulations. Their overall finding is that in storm conditions the empirical Poynting flux models tend to underestimate the flux while the models and simulations typically overestimate JH as the main ionospheric yield of the incoming flux. Furthermore, the positioning of modeled Q_E patterns appear to be randomly shifted against each other and against the observed Poynting flux energy input.

Table 1 shows Q_E values collected from the above-mentioned studies and from a few of other JH studies on regional and global scales. Typical upper limits of the Q_E estimates are in the range 10–60 mW/m^2. Similarly, as in the studies of Palmroth et al. (2005) and Rastätter et al. (2016), the results show big variability both in the peak values and in the spatial distribution of Q_E. For example, in the statistics by Olsson et al. (2004) and Weimer (2005) the peak values from the latter are roughly twice the values by the former. Both approaches show a tendency of high JH rates in the afternoon sector of the auroral oval, but otherwise their MLT-MLAT distributions are rather different. ISR measurements show enhanced Q_E in the dawn and dusk or afternoon sectors of the auroral oval (Aikio and Selkälä, 2009; Zhan et al., 2021) which is consistent with the results by Chun et al. (2002) for geomagnetically active times. However, ISR data as local observations cannot be used to validate the region of enhanced Q_E in the polar cap that appears in global empirical models of Q_E (Weimer, 2005; Zhang et al., 2005). Besides the high Q_E values from the storm time studies by Rastätter et al. (2016) two exceptions of the typical 10–60 mW/m^2 range in Table 1 are the results by GUMICS-4 and by AMIE as reported by Palmroth et al. (2005). The exceptionally low values by GUMICS-4 have their roots in the weak field aligned currents, particularly in the Region-2 part where non-MHD processes are involved. As emphasized later in the paper, this can be correlated also with the prevalence of JH in low conductance areas, like the Region-2 downward field-aligned current (FAC) in the afternoon/evening auroral oval. At the other end, methods that extract information on electric field and conductances from different independent sources, like AMIE, can generate some regional overestimates on JH rates, because they may not reproduce the spatial anticorrelation of the two parameters – **E** and Σ – correctly (c.f. Appendix in Palmroth et al. (2005)).

Table 1 includes also two rocket experiments, reported by Evans et al. (1977) and Sangalli et al. (2009). While rocket investigations of Q_E are rather scarce, not the least because of the large variety of data that need to be measured, such in-situ observations complement radar data and are essential for the comprehensive understanding of JH. To

Table 1

.

Reference	Scale	Method	Range of Q_E	Locations of enhanced Q_E
Evans et al. (1977)	Local	Bright auroral arc case study; Rocket observations of electric field and electron density above ~200 km, modeled ion-neutral collision frequency	up to 18 mW/m^2	Auroral oval MLAT ~68 MLT ~22
Chun et al. (2002)	Global	Statistics based on AMIE runs	up to 60 mW/m^2	Auroral oval MLTs 03–06
Olsson et al. (2004)	Global	Statistics based on LEO Poynting flux	up to 9 mW/m^2	Auroral oval MLTs 08–12
Weimer (2005)	Global	Statistics based on DE-2 Poynting flux	up to 20 mW/m^2	Auroral oval MLTs 14-18 and 03–07
Palmroth et al. (2005)	Global	Substorm case study; SuperDARN and Polar UV and X-ray data	up to 17 mW/m^2	Auroral oval MLTs 14–21, polar cap
Palmroth et al. (2005)	Global	Substorm case study; AMIE	up to 106 mW/m^2	Auroral oval MLTs 22–24 and 04–08
Palmroth et al. (2005)	Global	Substorm case study; GUMICS-4	up to 0.5 mW/m^2	Auroral oval MLTs 22–24, polar cap
Zhang et al. (2005)	Global	Empirical model of Q_E based on statistics of E, B and Σ_p	up to 25 mW/m^2	Auroral oval MLTs 14–17, polar cap
Aikio and Selk$\grave{}$al$\acute{}$a (2009)	Local	Statistics based on Σ_p and E from EISCAT mainland data	up to 14 mW/m^2	Auroral oval MLTs 03–06 and 18–20
Vanhamäki et al. (2009)	Regional	Omega band case study; regional KRM method	up to 14 mW/m^2	Auroral oval MLTs 04–05
Sangalli et al. (2009)	Local	Faint arc case study; Rocket observations down to ~90 km of all relevant data, neutral wind included	0.38 or 0.50 mW/m^2 with or without neutral wind	Auroral oval MLAT ~67 MLT ~02
Cai et al. (2016)	Local	Statistics on afternoon hot spots; Σ_p and E from EISCAT Svalbard data	up to 10 mW/m^2	Auroral Oval MLAT ~ MLT ~15
Rastätter et al. (2016)	Global	Storm case study; MHD simulation	up to ~250 mW/m^2	Auroral Oval dawn sector
Zhan et al. (2021)	Regional	Statistics on fall equinox conditions; Σ_p and E from Poker Flat AMISR, neutral wind included	up to 20–22 mW/m^2	Auroral Oval MLTs 04–06 and 16–19, Q_E larger in the evening sector
Kavanagh et al. (2022)	Local	Statistics based on Σ_p and E from EISCAT mainland data	up to 2.3 mW/m^2	Auroral oval MLTs 01–03 and 16–28

our knowledge, the early experiment of Evans et al. (1977) is the first rocket exploration of JH, addressing a broad and stable evening auroral arc during the recovery of a strong substorm. The data at and around the arc, mostly collected above 200 km, provide a remote sensing, height-integrated perspective, similar in this sense to the observations by Swarm. Unlike that, the more recent experiment of Sangalli et al. (2009) collected data down to ~90 km and was thus able to resolve the height variation of JH rate and of the primary data needed to derive it. Moreover, Sangalli et al. (2009) observed also the neutral wind and were able to quantify that by neglecting it Q_E increases from 0.38 mW/m^2 to 0.50 mW/m^2. The variation of 28% is consistent with the finding of Aikio et al. (2012), pointed out above. Note also the much smaller JH values compared to Evans et al. (1977), presumably related to the different energetics of the early morning faint arc, observed during the recovery of a moderate substorm.

Like described above, the global pattern of Q_E at high latitudes is known from statistical models and its dynamics have been characterized in case studies with MHD simulations and by combinations of global data sets. Although these studies provide information on typical Q_E intensities and on the regions of Q_E enhancements, global behavior of Q_E e.g. during substorms is not known to the same extent as we know the patterns of auroral current systems or auroral precipitation. In this paper we investigate the opportunities to use regional observations to bridge this gap in our knowledge. LEO satellite observations with electric and magnetic field data, like in the ESA Swarm mission (Friis-Christensen et al., 2006), can help in validation of MHD simulations. Another way is to use the combination of ground-based magnetic field and optical data. In this study we show how these two approaches can be combined to collect Q_E estimates as reference material for MHD simulations. Sections 2 and 3 below describe the observations, their analysis methods and the simulations used in this study. Our test event is presented in Section 4 and Q_E estimates are discussed in Section 5 and 6. Section 7 closes this paper with some discussion and conclusions.

2. Observations and data analysis methods

2.1. Ground-based data and analysis tools

We use the regional version of Kamide-Richmond-Matsushita (KRM) method developed by Vanhamäki and Amm (2007) to estimate Q_E in the area covered by an auroral camera equipped with a fish-eye lens (circular area of approximate diameter of 400–600 km). This approach assumes that ionospheric conductances can be derived e.g from optical data. Conductance data are combined with estimates of ionospheric equivalent currents which are derived with the method of Spherical Elementary Current Systems (SECS, Amm and Viljanen, 1999) as applied to ground-based magnetometer data. In this study we use All-Sky Camera (ASC) data from the EMCCD-camera (Sangalli et al., 2011) located at Kilpisjärvi (KIL; MLAT=66°, MLT=UT+2.5). SECS analysis is applied to the data of the IMAGE magnetometer network (Tanskanen, 2009). As outputs, regional KRM yields the electric field and ionospheric horizontal currents in the ASC field-of-view. By combining the

electric field with the ASC-based Pedersen conductance estimate, Q_E can be derived in the same area.

2.2. Swarm satellite data and analysis tools

The ESA Swarm satellite mission was launched in November 2013. It consists of three satellites in polar Low Earth Orbits (LEO). In 2017 the Swarm A and C satellites flew side-by-side at the altitude of 450 km, and the third satellite, Swarm B, flied at an altitude of 510 km. In this study we use measurements by the Swarm A and C magnetic field instruments (Vector Field Magnetometer, Tøffner-Clausen et al., 2016) and by the Swarm A electric field instrument (Thermal Ion Imager TII, Knudsen et al., 2017) for ionospheric parameters. The magnetic field data are used to estimate Field-Aligned Currents (FAC) by single-satellite and multi-satellite methods (Ritter et al., 2013; Blagau and Vogt, 2019; Vogt et al., 2013). The primary TII data are ion velocities, $\mathbf{V}_i$, used to derive the electric field by $\mathbf{E} = -\mathbf{V}_i \times \mathbf{B}$, with $\mathbf{B}$ the magnetic field. Since the along-track ion velocities are computed as differences between two large quantities, the observed and the satellite airspeed /RAM, they are affected by significant errors, which result in low accuracy of the zonal, cross-track electric field. Consequently, in this study we only use the meridional, along-track electric field, derived from the observed cross-track ion velocities. The time resolution of E and B data is 1 s. Auxiliary data for precise orbit determination of Swarm A are used to estimate thermospheric density variations (Swarm L2 product DNSAPOD) as response to enhanced JH.

In principle, Swarm **E** and **B** data can be used also for deriving the ionospheric conductance, via the SECS technique, as described by Amm et al. (2015). The procedure is simpler for 1D arc events (where variations in longitude are significantly smaller than those in latitude), like the one in this paper, when data from just one satellite, like Swarm A, are enough. However, in our particular event (and many other 1D events, mostly observed under low activity conditions), the ionospheric current turned out to be too weak for reliable SECS results, which prompted the use of ground data.

3. Simulations

We use in this study three different simulation codes to estimate the time and space variations of Q_E in the Northern hemisphere during our test event on Jan 4, 2017. Two of the simulation codes, GUMICS-5 (Honkonen et al., 2022) and SWMF (Tóth et al., 2005, 2012), concentrate purely on plasma physics in the coupled solar wind – magnetosphere – ionosphere system. The third code, CTIPe (Codrescu et al., 2012), addresses ionosphere-thermosphere interactions as driven by solar and magnetospheric activity. The inputs used by the three codes and the outputs discussed in this study are summarized in Fig. 1 and more detailed descriptions of the simulations are given in the following subsections.

3.1. GUMICS-5

GUMICS-5 solves the ideal MHD equations in near-Earth space region which extends to ±248 R_E in X direction in geocentric solar ecliptic (GSE) coordinates, where $R_E = 6371$ km is the radius of Earth. In GSE Y and Z directions the simulation extends to ±64 R_E. In this study we use magnetospheric resolution of 0.25 R_E up to distances of 13 R_E from the Earth and a decreasing resolution further away down to a minimum of 8 R_E. GUMICS uses dynamic time step which is derived from the solution computed during previous time step and is based on wave propagation speeds away from cell interfaces and the sizes of these cells. GUMICS also uses temporal subcycling but typically the smallest time step is between 10 and 100 ms. The ionosphere is modeled as a spherical surface and is discretized as a static triangular grid with a maximum resolution of approximately 100 km everywhere poleward of ±58° in magnetic latitude. In this study we use ionospheric solutions with 1 min resolution. For more details about GUMICS-5, see Honkonen et al. (2022) and Janhunen et al. (2012).

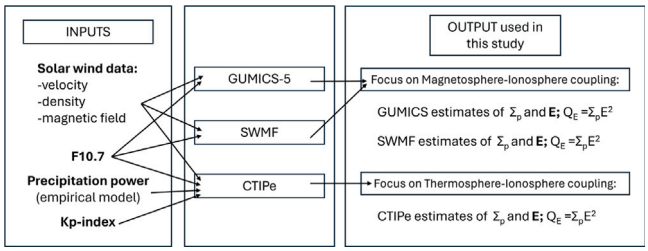

Fig. 1. A diagram summarizing the inputs of the simulation codes whose results are discussed this study.

Ionospheric electrodynamics of GUMICS is governed by FACs and estimated electron precipitation mapped from the inner boundary of the magnetospheric grid, at 3.7R_E. The energy flux of electron precipitation is estimated from the temperature of magnetospheric plasma with a Maxwellian distribution. The precipitation is assumed to cause ionospheric ionization whose production rate depends on the magnetospheric plasma temperature and density and on the loss cone filling rate, which is an adjustable parameter between 0 and 1 (in this study: 1 around the poles, 0.01 around the equator, with a smooth rapid decrease around 67° MLAT). The altitude profile of ionospheric electron density is solved from the ionospheric continuity equation. The electron density is then used to derive altitude integrated Hall and Pedersen conductivities. The thermospheric parameters needed to derive the conductances (e.g. the ion-neutral collision rates) are taken from the MSIS model (Hedin, 1991). The ionospheric height integrated Ohm's law and the ionospheric current continuity equations can be combined to a differential equation from which the electric potential is solved (for more details, see Janhunen et al. (2012)). In this approach, the magnetospheric parameters controlling the spatial distribution of ionospheric conductances and electric field are vorticity of the perturbed part of the magnetic field (as input for FACs) and plasma temperature and density.

3.2. Other simulations

We compare GUMICS-5 results with Space Weather Modeling Framework (SWMF, Tóth et al., 2005, 2012) simulations using the Global Magnetosphere (GM) and Ionospheric Electrodynamics (IE) components. The GM module is based on the BATS-R-US MHD code (Powell et al., 1999; Gombosi et al., 2013) with the finest grid resolution of 0.25 R_E. The explicit time step in the simulation is typically about 0.07 s. The magnetospheric inner boundary is at the distance of 2.5 R_E from the Earth center. The mapping from GM to IE is done with an analytic formula assuming a tilted dipole field. The IE module is a height integrated spherical surface at the altitude of 110 km. The ionospheric electric potential is solved from the basis of FACs as the input from GM. In this study we use ionospheric results with 5 min resolution. FACs are related with ionospheric Hall and Pedersen conductances using an empirical model (Ridley et al., 2004) which has exponential form and parameters determined from the output of the AMIE assimilative mapping tool (Richmond and Kamide, 1988). The AMIE tool has been run with the input by an extensive network of ground-based magnetometers.

In addition to GUMICS-5 and SWMF, which both are codes with the focus on magnetosphere-ionosphere coupling, driven by solar wind properties, we have used in this study also the Coupled Thermosphere Ionosphere Plasmasphere electrodynamics (CTIPe) model (Codrescu et al., 2012), which is a composition of four different sub-models: a global thermosphere model, a high-latitude ionosphere model, a mid-

and low-latitudes ionosphere/plasmasphere model and an electrodynamical calculation of the global dynamo electric field. The thermosphere model is run with 1 min time step and the ionosphere/plasmasphere model is run with 5 min time step. The inputs of CTIPe are F10.7 cm radio flux, IMF magnitude and clock angle, solar wind velocity and proton density, geomagnetic activity level (Kp index), and total hemispheric precipitation power. The precipitation power is estimated with an empirical model based on NOAA POES satellite data binned according to solar wind properties. The CTIPe outputs of relevance for this study include Q_E, conductivities, neutral and electron densities and electron temperature. The altitude range covered by the model varies for the different output parameters. Ionospheric properties are modeled up to Swarm A and B altitudes, while neutral atmospheric parameters are available for altitudes <350 km. The resolution of CTIPe results is 2° in latitude, 18° in longitude and 15 pressure levels in vertical direction. JH in CTIPe has two parts, one driven by the average convection electric field and the other driven by a random component, representing small scale sub-grid variability in the convection electric field (Codrescu et al., 1995, 2000).

4. The event: Jan 4, 2017 16:00–24:00 UT

Solar wind observations by the ACE and DSCVR satellites (Zwickl et al., 1998; Loto'aniu et al., 2022) on Jan 4, 2017 are shown in Fig. 2. The satellite data show a front of high proton density during the morning hours of the day after which the solar wind speed started to increase gradually from values below 400 km/s to the range of 480–550 km/s. During the afternoon and evening hours the solar wind proton density stays rather stable in the range 7–10 cm^{-3}. After 12 UTC the Interplanetary Magnetic Field (IMF) By stayed mostly in negative values, while IMF Bz was positive, except for some excursions to negative values during 17–20 UT. These excursions caused an enhancement in geomagnetic activity, which is seen in Fig. 3 as an increase of the AE-index (Davis and Sugiura, 1966) to values close to 1000 nT during 18:30–20:00 UT. Fig. 3 shows also a GUMICS-5 simulation of the AE-index. The substorm activity after 18:30 is beyond the reach of GUMICS-5, but before and after the substorm the GUMICS-5 simulation of the AE-index follows quite nicely the time variations in the real AE, but the intensities are underestimated by factor of 3.6. Scaling with this factor provides the exact match of the simulated and observed AE at 18:32, during the Swarm A crossing of the nightside auroral oval a few minutes before the substorm onset.

Fig. 4 shows the overflights of the Swarm A and C satellites above the Northern hemisphere during the evening of Jan 4, 2017. The overflight at 18:30–18:35 over Finland has been used in our Q_E assessment on regional scales. In the analysis of global Q_E activity by simulations, we have used times from five overflights during the same evening (times shown in Fig. 3 with vertical dashed lines).

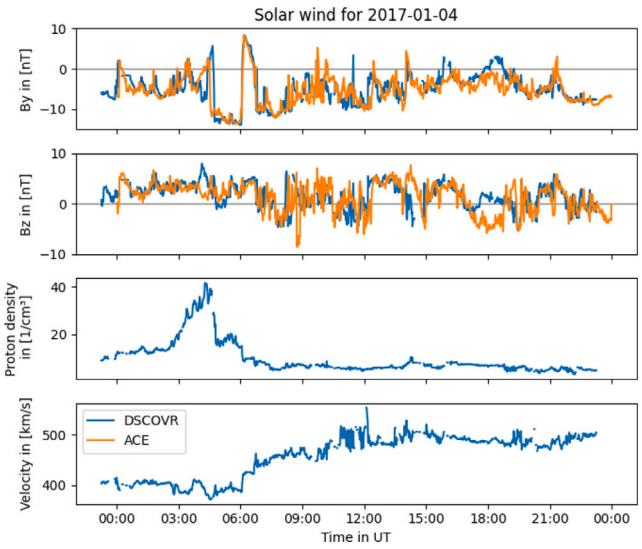

Fig. 2. Solar wind observations by the ACE (orange) and DSCVR (blue) satellites on Jan 4, 2017. ACE data have been used as input for the simulations of this study. The timing of DSCVR observations has been shifted so that it matches with the ACE data. (For interpretation of the references to color in this figure legend, the reader is referred to the web version of this article.)

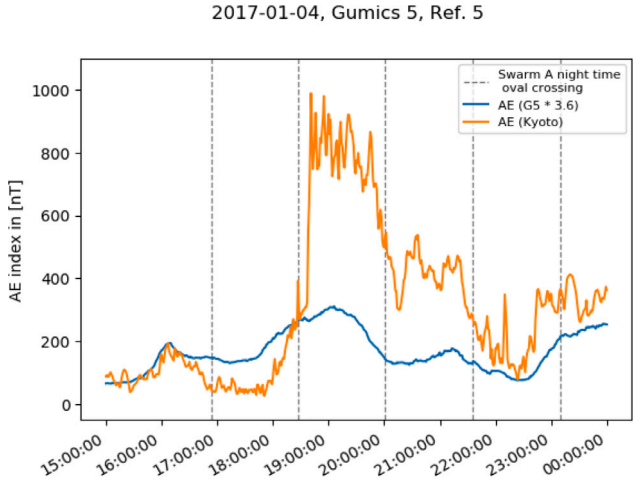

Fig. 3. AE-index variations during the evening of Jan 4, 2017 (orange curve). AE-estimate by the GUMICS-5 simulation (as multiplied by factor 3.6) is shown with the blue curve. Times of Swarm A nightside oval crossings are shown with the dashed vertical lines. (For interpretation of the references to color in this figure legend, the reader is referred to the web version of this article.)

5. Q_E estimates by ground-based and Swarm data

5.1. Ground-based data

Fig. 5 shows a Pedersen conductance estimate as derived from the KIL ASC image acquired at 18:32 UT. The conductance map can be used together with IMAGE magnetometer data from the same time instant in the regional KRM-analysis. As support for ASC data in this study we have used EISCAT conductances from the data base maintained by the Japanese National Institute of Polar Research (http://esr.nipr.ac.jp/www/eiscatdata/conductivity.html). The EISCAT data used for our empirical conductance modeling are height-integrated conductivities measured between November 2012 and March 2017, selected for the days when aurora was visible by the camera (clear sky). The empirical relation thus obtained is: $\Sigma_P = 0.056 I^{0.52}[S]$ where I is the aurora intensity at 557 nm in Rayleighs [R] as obtained from the ASC picture. Raw counts recorded by the camera have been converted to intensities using data from a calibration session of the camera in September 2016. The Pedersen conductance values achieved with our approach are similar – typical values around 5–10 S – to the values reported by Juusola et al. (2016) in their auroral arc study utilizing the SECS-Swarm variant by Amm et al. (2015).

Radial current as derived with our KRM approach at the Swarm A ionospheric foot point locations is shown in Fig. 6 together with the Swarm field-aligned current product (FACATMS_2F) from Swarm A magnetic field data. The intensity of auroral luminosity is shown in the Figure as reference information. KRM and Swarm A TMS yield mutually rather consistent estimates about the peak upward current (~1.8–2.0 A/km^2) at the poleward edge of the auroral system of 2–3 arcs, which supports the anticipation of KRM giving sensible results also for Q_E. The downward closure current is less clear in the results. Both methods give hints on downward currents on both sides of the arc system, but their intensities and latitudinal distributions

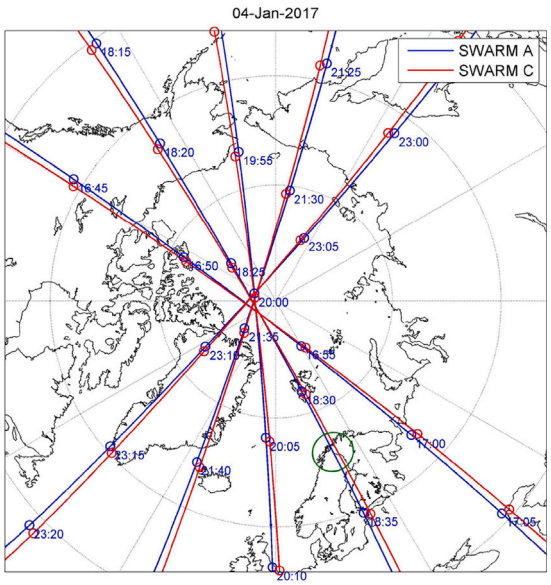

Fig. 4. Swarm A and C overflights in the Northern hemisphere during the evening hours of Jan 4, 2017. The field-of-view of Kilpisjärvi (KIL) all-sky camera at 110 km altitude is shown with the green circle. (For interpretation of the references to color in this figure legend, the reader is referred to the web version of this article.)

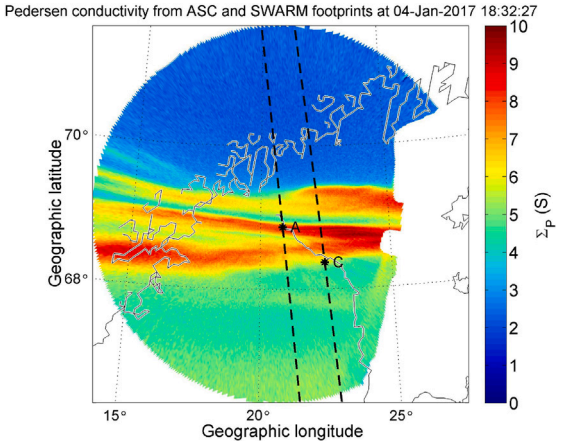

Fig. 5. Pedersen conductance derived from ASC intensity during the Swarm A and C overflight above the Kilpisjärvi ASC on Jan 4, 2017 around 18:30 UT.

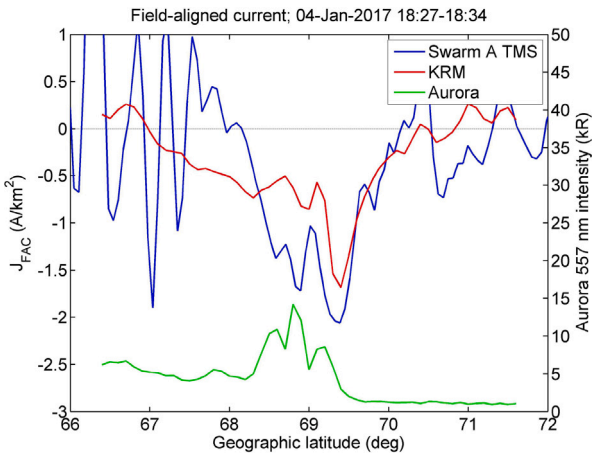

Fig. 6. Radial current estimates by the regional KRM method (red curve) and the L2 Swarm A single satellite time series (TMS) product (blue curve) in the vicinity of the evening sector auroral arc system shown in Fig. 5. Positive radial currents can be related with upward FAC. (For interpretation of the references to color in this figure legend, the reader is referred to the web version of this article.)

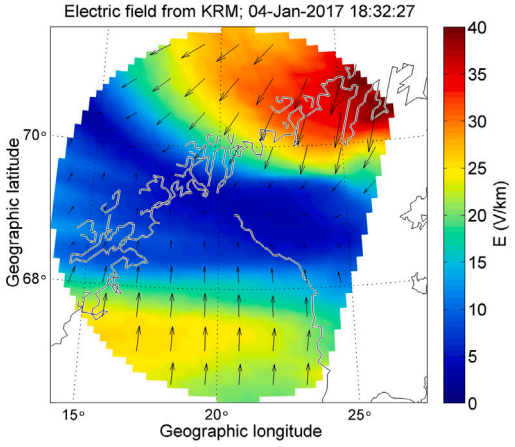

Fig. 7. Electric field in the vicinity of the arc system of Fig. 5 as estimated by the regional KRM method.

differ significantly from each other. Considering also the magnetic field perturbation (Fig. 9 below), most of the downward current is observed at lower latitudes, separated from the upward current by a region of diffuse aurora (the green area in Fig. 4, south of the arc system) and small scale variable FAC, with little overall effect on the magnetic field.

Fig. 7 shows the spatial distribution of **E** in the vicinity of the arc system as derived with the KRM method. In the case studies of evening sector auroral arcs by Aikio et al. (2002), enhanced northward electric field is measured by EISCAT particularly on the equatorward side of the arc, while on the poleward side the northward field is weaker or even negative. In our case **E** is northward on the equatorward side of the arcs and directed south to south-west on their poleward side. The KRM based field intensities, 15–30 V/km outside of the arcs, are somewhat smaller than the EISCAT based values (20–90 V/km) reported by Aikio et al. (2002). The reversal of the electric field together with the low conductance north of the arc system suggest that this is observed at the convection reversal boundary, collocated here with the polar cap boundary, which is not uncommon in the evening sector. The observed profile of the electric field is presumably the result of the large scale convection pattern, with plasma velocity changing sign in the arcs' region, combined with the smaller scale effect of polarization, due to enhanced conductance at the arcs.

The distribution of Q_E in the KIL ASC field-of-view is shown in Fig. 8. The largest Q_E values by KRM appear on the southern side of the arc and in the top right corner of the ASC field-of-view. As the Swarm satellites do not cross the latter region and thus KRM results cannot be confirmed by satellite observations, we concentrate in our analysis to the Q_E values on the southern side of the arcs (up to 3.5 mW/m^2) which are similar to the medians in the EISCAT ISR statistics by Aikio and Selkälä (2009) and the medians of afternoon hot spots (for positive IMF Bz) as reported by Cai et al. (2016). The KRM based Q_E estimates for the auroral omega bands by Vanhamäki et al. (2009) are clearly higher (6–14 mW/m^2) than those reported here, in consistence with observations of omega bands mainly in the morning and during substorm recovery, different from the substorm growth in the evening sector reported here. It is interesting to compare our estimates of energy dissipation by JH with some estimates of the other dissipation mechanism related with auroral structures, namely dissipation by particle precipitation. Particle precipitation energy fluxes reported by Partamies et al. (2004) for auroral arcs are 4–6 times larger than the Q_E values from our KRM analysis. This finding is somewhat surprising, because in global scales JH is known to be a more efficient

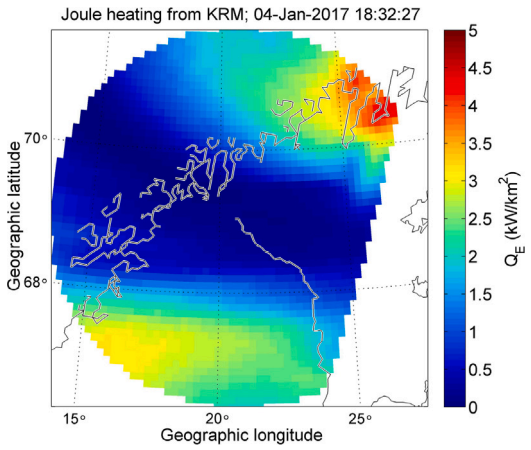

Fig. 8. Q_E in the vicinity of the arc system of Fig. 5 as estimated with the regional KRM method using ground-based magnetometer and ASC data.

way of energy dissipation than auroral precipitation (Chun et al., 2002). The regional KRM analysis shown here, as well as that by Vanhamäki et al. (2009) indicate enhanced Q_E values in the regions of low Pedersen conductances. This feature is consistent with a current generator model of the auroral current circuit (Lysak, 1985; Vogt et al., 1999) and is observed also in simulations (see Section 5.2). Its importance for global estimates of the energy budget and for the need of future measurements is addressed further in the Discussion Section.

5.2. Swarm data

Fig. 9 shows the magnetic field perturbations observed in-situ by Swarm A and C (top panels) together with the respective FAC densities in the North – East – Center of the Earth (NEC) reference system. The estimated FAC density agrees well with the optical data, in that the equatorward edge of the arc is also the equatorward edge of the upward FAC. The FAC density is also consistent with the regional KRM results (Fig. 6). The upward FAC reaches in both cases a maximum value close to 2 A/km^2. The spatial profile is similar too, with upward FAC extending from ~68–70° geographic latitude and maximum near 69°. The larger Swarm coverage in latitude, as compared to the regional KRM, provides also a better view over the complete current system, with the region of diffuse luminosity in Fig. 5 corresponding to the broad plateau in magnetic perturbation between the poleward Region 1 upward FAC and the equatorward Region 2 downward FAC. These large-scale currents are easier to distinguish from the dB plots in the top panels of Fig. 9, where Region 1/Region 2 current is indicated by the prominent positive/negative slope of dB_C. Small-scale currents are visible particularly in the bottom panels of Fig. 9. They show great variability in their direction and intensity at the latitudes of the R2 current. The stronger tendency for filamentation of downward currents when compared with upward currents has been pointed out also by Elphic et al. (1998).

A closer look over the estimation of Q_E along Swarm A footprint, while crossing the KIL ASC field-of-view, is presented in Fig. 10. Since the electric field accuracy is better on Swarm A than on Swarm C, Swarm A is also the better choice for estimating Q_E. The plot shows the zoomed-in magnetic perturbation, the electric field from Swarm A (E_x) and by the regional KRM technique (E_x and E_y), the conductance inferred from optical data, and finally Q_E. The low accuracy zonal electric field, E_y, derived from Swarm data, is not shown (see Section 2.2).

Considering how different the observations and data processing techniques are, a most remarkable feature is the good match of the Swarm A and KRM E_x – consistent with the good agreement between KRM radial current (Fig. 6) and Swarm A FAC (Fig. 9). These consistency checks validate also the conductance proxy inferred from optical data, used as input to KRM technique. Note also the reversal of E_x from southward to northward (while moving southward with the satellite) at the poleward edge of the arc region, already pointed out in the previous section. Considering the evening MLT of 20.3 (bottom of Fig. 10) and the missing auroral luminosity north of the arc (in contrast to the diffuse luminosity south of the arc), this indicates that the poleward edge of the arc system was also the polar cap boundary, rather typical for the local time and stage of the substorm cycle. While local polarization effects inside the arc system cannot be excluded, the drop in the electric field and Q_E appears to be closely related to the large-scale plasma convection pattern (see also Figs. 7 and 8).

As expected from the electric field profiles, Q_E is dominated by E_x contribution and shows similar trends in the ground and satellite estimates. Enhanced Q_E occurs south of the arc, where both the electric field and conductance are significant. In this region, the plateau in the magnetic perturbation indicates small average FAC and dominant ionospheric current related to the closure of the large scale FAC system. Q_E reaches a maximum value of ~4 mW/m^2 (in satellite data), just south of the arc, in the lower half of the range provided by Table 1, Considering that the event was observed a few minutes before the substorm onset, when AE was just 250 nT (Fig. 3), this value looks fairly reasonable. The rapid increase of the electric field and conductance around the onset time may well explain the enhanced Q_E provided by simulations during the substom later on (see next section), when AE reaches ~1000 nT.

Based on the 1D symmetry of the event, as observed in the optical data and in the similar magnetic perturbations at Swarm A and C (Fig. 9), one can infer from the Q_E profile an average value of ~1.4 mW/m^2, about equal along the ionospheric footprints of both Swarm A and C. Assuming steady state (as indicated by optical data)

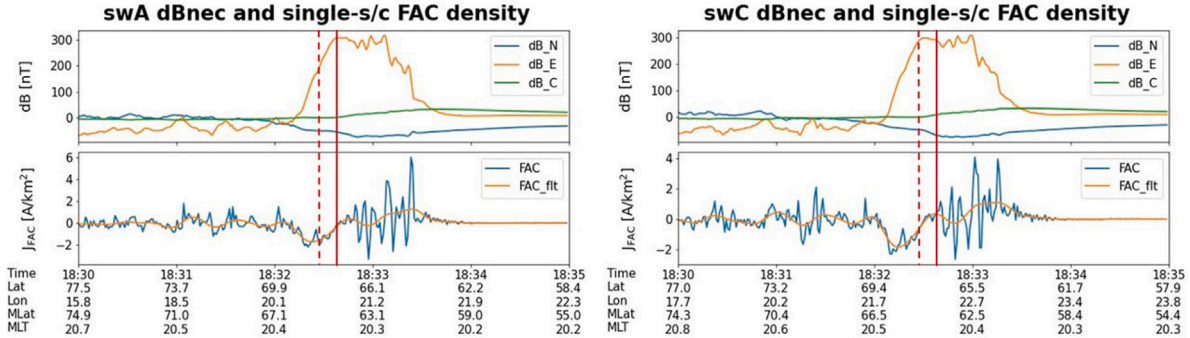

Fig. 9. Magnetic field perturbation (North-East-Center coordinate system) and FAC density (1 Hz and filtered) for Swarm A (left) and Swarm C (right). The dashed and solid vertical lines indicate 18:32:27 and 18:32:37 UT, respectively, the times when Swarm C (Fig. 5) and Swarm A reach the equatorward edge of the arc system and of the upward FAC.

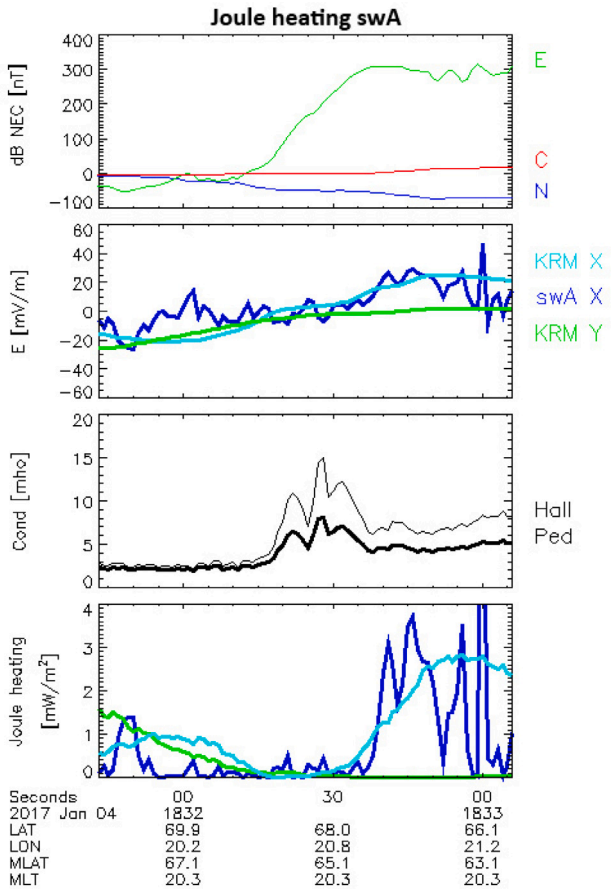

Fig. 10. Q_E inferred from ground and Swarm A data while crossing the KIL field-of-view. From top to bottom: magnetic perturbation, electric field from Swarm data (E_x blue) and from regional KRM (E_x cyan, E_y green), Pedersen (bold) and Hall (thin) conductance from optical data, Q_E (same color code as electric field). (For interpretation of the references to color in this figure legend, the reader is referred to the web version of this article.)

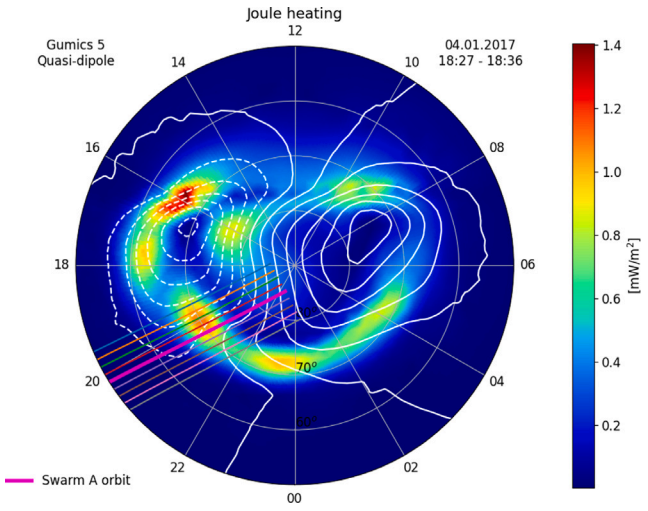

Fig. 11. GUMICS-5 results on Q_E spatial distribution in MLT-MLAT coordinates (Northern hemisphere, average from time period 18:27–18:36 UT). The track of Swarm A across the evening sector auroral oval around 18:30 is shown with the thick purple line. The lines of other colors show tracks shifted slightly in geographic longitude from the Swarm A track. The white lines show equipotential contours or convection streamlines. (For interpretation of the references to color in this figure legend, the reader is referred to the web version of this article.)

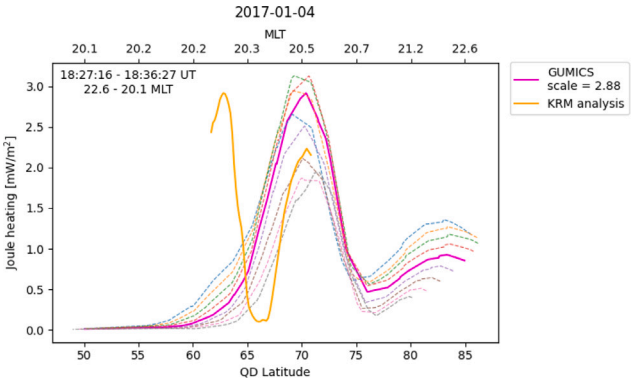

Fig. 12. Comparison of Q_E extracted from GUMICS-5 (thick purple line) and KRM (thick orange line) analyses. GUMICS results have been multiplied with a factor of 2.88. Dashed lines of different colors correspond to the tracks shown in Fig. 11. Note the magnetic (quasi-dipole) latitude on the x axis, to be compared with Fig. 10 (both magnetic and geographic latitudes) and Fig. 8 (geographic latitude). (For interpretation of the references to color in this figure legend, the reader is referred to the web version of this article.)

during the ~80 s Swarm crossing over the KIL field-of-view, one can derive an integrated JH of ~46 MW over the area of ~550 × 60 = 33,000 km^2 between the two satellite footprints, as well as a total energy of ~1000 kW h – of the order of a household consumption over one year.

6. Simulation results

6.1. Q_E Estimates by GUMICS-5 compared with KRM and SWMF

The spatial distribution of Q_E in the Northern hemisphere by GUMICS-5 is shown in Fig. 11. The track of the Swarm A overflight during the crossing over the KIL ASC field-of-view is shown in the Figure with the purple line. According to the simulation, Swarm A crossed the auroral oval close to the transition region between the evening and morning sector convection cells. The Q_E values at the Swarm A oval crossing are enhanced, but not as high as the simulation yields for the localized Q_E enhancement in the late afternoon sector at 16 MLT. GUMICS-5 shows also significant Q_E values in the polar cap, which is a similar feature to the empirical models by Weimer (2005) and Zhang et al. (2005). Q_E along the Swarm A trajectory as extracted from KRM and from GUMICS are compared in Fig. 12 as functions of magnetic latitude. The latitudinal distributions of Q_E from these two approaches are different from each other, most likely because MHD cannot reproduce arc scale structures in the ionosphere. In addition, it seems that GUMICS locates the evening sector auroral oval to latitudes higher by ~5 degrees than the latitudes according to our ground-based observations. GUMICS-5 gives Q_E peak values that are smaller than those from the KRM analysis by a factor of 2.88 that is rather close to the factor of 3.6 which was used in Fig. 3 to get the GUMICS-based and observed AE-indices matching with each other. This may reflect the close relationship between Q_E and AE, via the Pedersen and Hall components, respectively, of the ionospheric current, both driven by the same ionospheric electric field.

GUMICS-5 results on Q_E are compared with those by the SWMF simulations (Tóth et al., 2012) in Fig. 13. The JH rate values along Swarm A track are higher by SWMF (maximum ~ 1.5 mW/m^2) than those by GUMICS-5 (~1 mW/m^2). Also in the global view, SWMF gives somewhat larger values than GUMICS (maximum values of ~2 and of ~1.5 mW/m^2, respectively). The spatial distributions of JH rates are different too. SWMF shows two distinctive regions of enhanced Q_E, one at the noon and the other in the pre-midnight sector. In GUMICS-5 Q_E enhancements are more sporadically distributed. The high Q_E on the night side part of the oval is at higher latitudes in SWMF than in

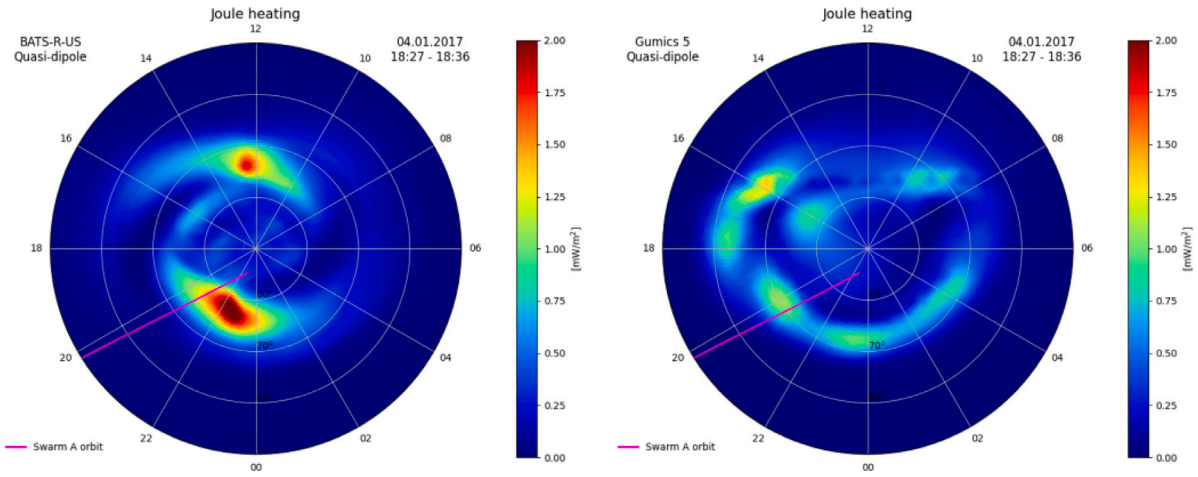

Fig. 13. Q_E simulated by SWMF (left) and by GUMICS-5 (right), in MLT-MLAT coordinates, Northern hemisphere (averages from time period 18:27–18:36 UT). The Swarm-A track across evening sector oval is marked with the thick purple line (c.f. Figs. 11 and 12). The GUMICS-5 result on the right is similar to Fig. 11, just with different color scale, for better comparison with SWMF. (For interpretation of the references to color in this figure legend, the reader is referred to the web version of this article.)

GUMICS-5. Around noon the situation is opposite: SWMF gives high Q_E at MLATs 70–75, while in GUMICS slightly enhanced Q_E is located at MLAT ~80. The "hot spot" of QE at MLT 16, dominating in the GUMICS-5 results, is missing from the SWMF results. Both simulations show slightly enhanced Q_E in the polar cap (here estimated to be at latitudes above MLAT 75).

For a better insight to the differences between SWMF and GUMICS-5 Q_E results, the distributions of Pedersen conductances and electric field intensities by the two simulations are shown in Figs. 14 and 15. From the formula of Q_E used in the simulations ($Q_E = \Sigma_p E^2$) it might be inferred that the distribution of **E** governs the distribution of Q_E, but it is good to recognize that Σ_p with its spatial variations affects significantly the solution of **E** in the simulated ionosphere. This impact is visible as clear anti-correlation between the two parameters in the simulation results. Such anti-correlation can be expected because enhanced Pedersen conductances facilitate closure of electric potential differences in the ionosphere and is in turn consistent with the current generator model of the auroral current circuit ($Q_E = J_p^2/\Sigma_p$ where J_p is the Pedersen current closing FACs in the ionosphere). This implies that the electric field adapts to the conductance, such that the (rather constant) ionospheric current matches the FAC driven by a magnetospheric current generator (as opposed to a voltage generator, where voltage – and electric field – would be imposed from the magnetosphere). We conclude that the differences in Q_E by SWMF and GUMICS come from the fact that Pedersen conductances are derived according to different principles in the two simulations. In SWMF, the distribution of Σ_p is closely linked with that of FACs, which are dependent on the curl of magnetospheric **B** at the magnetosphere–ionosphere interface boundary. In GUMICS, the magnetospheric plasma density and temperature control the distribution of Σ_p. At the time instant of our interest, the approach by SWMF gives high Σ_p at the prenoon and afternoon sectors of the auroral oval, while in GUMICS-5 Σ_p is enhanced particularly in the midnight sector.

The differences of GUMICS and SWMF in the noon sector Q_E have once again their roots in the differences of dayside Σ_p determination. Dayside conductances in both simulations are derived by square root summing of contributions by electron precipitation and solar UV illumination (Ridley et al., 2004; Janhunen et al., 2012). The latter is derived with the empirical model by Moen and Brekke (1993), which uses the solar radio flux F10.7 as its input. GUMICS uses as default the value of 100×10^{-22} W/m^2 Hz for F10.7, while in the SWMF run F10.7 has been 70×10^{-22} W/m^2 Hz. The two simulations have also some differences in their modeling of background conductances due to stellar and cosmic sources (for more details, see Ridley et al. (2004), Janhunen et al. (2012)).

6.2. Impact of Q_E enhancements on thermospheric density

During the evening of Jan 4, 2017 (16:30-23:30 UT) Swarm A crossed five times the night side auroral oval (c.f. Fig. 4). These crossings took place around MLTs ~20–21. Fig. 16 shows Q_E estimates (averages of Q_E over MLATs 50–85) from that same MLT sector by GUMICS-5, SWMF, and CTIPe. Consistently with the results shown above in Section 6, GUMICS-5 Q_E estimates are significantly smaller than those of the two other simulations. Therefore, GUMICS results have been multiplied with a factor of 4.14 to get them to the same level as the other estimates. In Fig. 16 we want to pay attention more to the time evolution of the Q_E estimates than to their absolute values. We compare time variations of regional Q_E in MLT 20–21 with time variations of neutral density which are known to be very large scale and globally coherent. Those are expected to correlate well with globally integrated Joule heating which correlates in turn with the AE-index (Ahn et al., 1983). In the top panel time evolution of simulated Q_E values are shown with the observed AE-index (same curve as shown in Fig. 3). In the bottom panel the Q_E values of the top panel have been smoothed by running averages over a time window of 90 min. These values are compared with estimates of thermospheric densities by the Swarm DNSAPOD product (averages over the satellite oval crossing).

Basically, the Q_E simulation results in the top panel of Fig. 16 are mainly related to the Pedersen current, while AE-index is dominated by the Hall current electrojet. As both currents are related to each other in the coupled Magnetosphere–Ionosphere system, one can expect some similarities in the time evolutions of the simulated Q_E estimates and the observed AE-index. However, the variations cannot be highly correlated because the simulated Q_E proxies in Fig. 16 have regional character, while AE is a global index. So, AE-index in Fig. 16 should be used mainly as a guide on the substorm evolution which in this case is rather typical with the growth phase roughly during 1800–1840 UT, expansion during 1840–1950 UT, and gradual recovery during 1950–2230 UT. A new intensification starts after 2230 UT. In the traditional substorm picture activity starts from the premidnight sector from where it then gradually moves to other MLT-sectors of the oval. All the three simulations show Q_E enhancements during the growth phase in MLT 20–21, which seems to be compliant with the standard picture. Interestingly, there is a time shift in the Q_E and AE growth phase increases so that the former precedes the latter with half and hour. This,

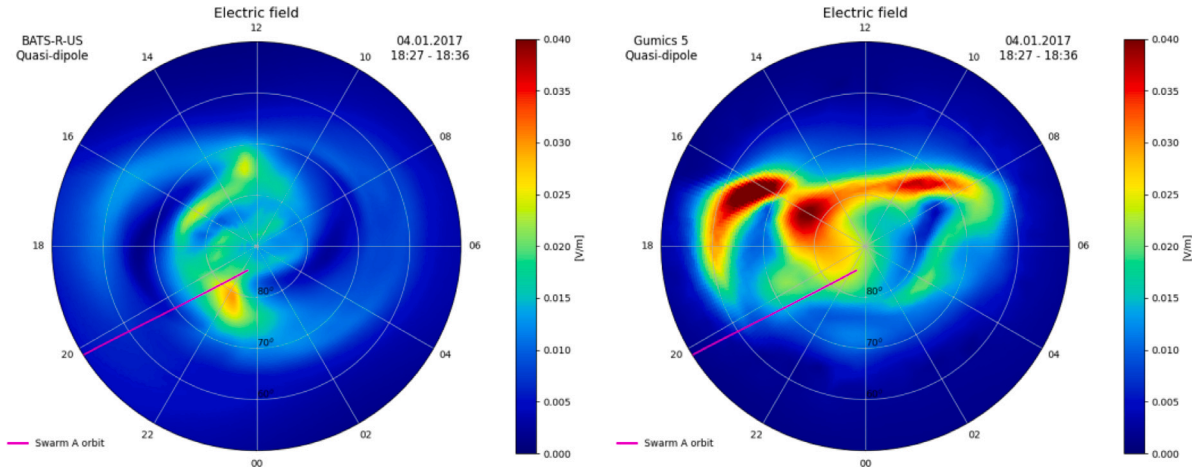

Fig. 14. Intensity of the electric field by SWMF (left) and by GUMICS-5 (right), MLT-MLAT, Northern hemisphere (averages from time period 18:27–18:36 UT).

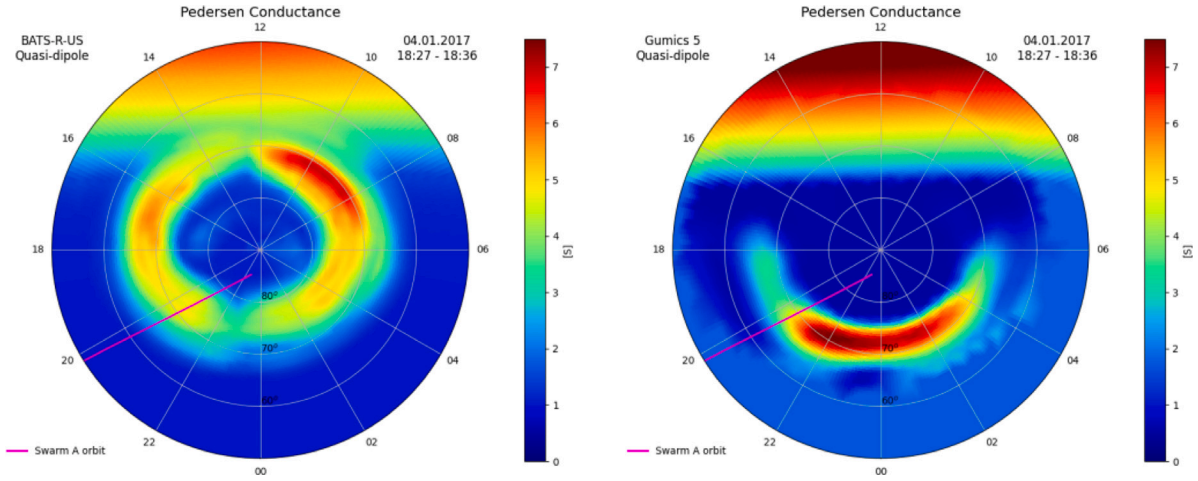

Fig. 15. Pedersen conductance by SWMF (left) and by GUMICS-5 (right), MLT-MLAT coordinates, Northern hemisphere (averages from time period 18:27–18:36 UT).

perhaps, can be interpreted so that the ionosphere Hall current system takes some time to develop while Joule heating increases as soon as the E field increases. For GUMICS the Q_E values during the growth phase are larger than anytime else during the studied period. The two other simulations show large heating rates in the evening sector also during the expansion and recovery phases. Consequently the time variations of Q_E are very different by the three simulations until the start of the new intensification, when their coherence reappears as gradually increasing heating rates in all three cases.

The expected deviations in the time variations of simulated Q_E estimates and observed AE as shown in Fig. 16 (top panel) have different characteristics in the three simulation cases. The GUMICS result (blue line) appears to follow rather well the AE index after ~18:30 UT, whereas Q_E by SWMF (green) and CTIPe (orange) show good correlation with AE just over the second half of the interval, after the substorm main phase. Note that Pedersen conductance in GUMICS and SWMF is the effect of (different) magnetospheric drivers (plasma density & temperature and field-aligned currents, respectively, as explained in Section 6.1), while CTIPe relies on the ion-neutral collisions at low altitude, which is indeed the direct cause of conductance. As CTIPe Q_E is not driven just by the average convection electric field but also contains a random component (c.f. Section 3.2), deviations in its time evolution from AE are more prominent than the deviations by the two MHD simulations. When CTIPe Q_E time variations are smoothed (bottom panel of Fig. 16) they become more consistent with the MHD results, particularly those by SWMF. GUMICS Q_E time evolution is remarkably different from the two other results, as it shows strongest heating at the substorm onset, while in the other results strongest heating takes place during the substorm recovery phase.

The bottom panel of Fig. 16 also shows the atmospheric density, as observed by Swarm for its five evening sector oval overpasses during 16:30-24:00 UT. Variations in density, smoothed by the large inertia of the neutral atmosphere, are compared on 'equal basis' with smoothed Q_E, which otherwise responds promptly to variations in the ionospheric electrodynamics. Swarm measured highest densities during the fourth overpass, which took place after the substorm at 21:40 UT. Compared to the value of the first overpass at 17:00, Swarm measured a density increase of ~20% as a consequence of the substorm activity. The Q_E proxy by CTIPe which shows steadily increasing heating during 17:00-20:15 UT seems to be more consistent with this finding than the Q_E time evolutions by the two other simulations. SWMF Q_E correlates also well with atmospheric density, except for the drop after the second Swarm pass. In GUMICS results the period of enhanced heating takes place clearly earlier and is shorter than in the two other simulations.

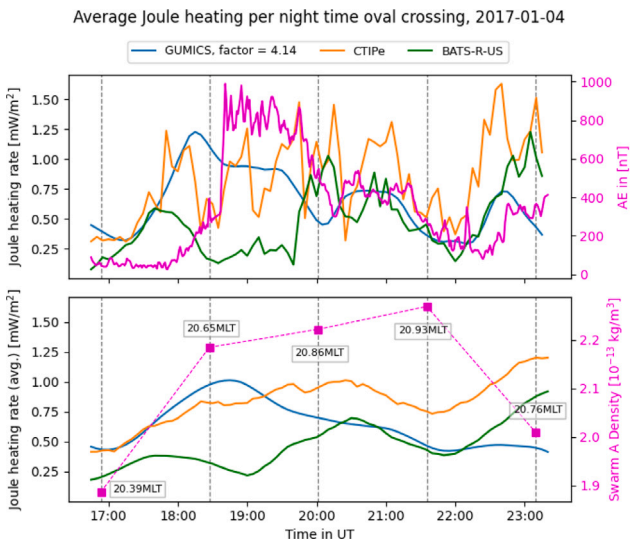

Fig. 16. (Top panel) Q_E estimates from the MLT sector 20–21 by GUMICS-5, SWMF, and CTIPe. The time resolution of simulation results used here is 5 min. The estimates are averages of Q_E over MLATs 50–85 with 1 degree resolution. As reference information also the observed AE-index is shown in the same plot (same curve as shown in Fig. 3). (Bottom panel) the Q_E values of the top panel as smoothed by running averages over a time window of 90 min. As reference information the plot shows also the estimates of thermospheric densities by the Swarm DNSAPOD product (averages during the satellite oval crossing).

7. Discussion

As presented above, differences in the GUMICS-5 and SWMF based Q_E estimates have their roots in the solutions how the simulations derive ionospheric conductances from magnetospheric parameters. Electron precipitation into the ionosphere needs to be estimated with some ad hoc approach, because the fluid approach in MHD does not provide information about electrons. The version of SWMF used in this study links electron precipitation with large scale FACs, while GUMICS-5 estimates precipitation from magnetospheric plasma density and temperature. Both these ways can be motivated, e.g., by the empirical formulas of Robinson et al. (1987), which link Pedersen conductance both with the number flux and average energy of precipitating electrons. The former is directly linked to FAC and the latter can be characterized with the temperature of Maxwellian plasma populations. Obviously, neither of the two codes takes into account fully these dependencies, with SWMF emphasizing the first, while GUMICS-5 the second. Based on our test case, the SWMF approach is better, in the sense that it does not underestimate Q_E values so strongly when compared with observations, as the GUMICS-5 approach does. However, ranking the simulations based on their Q_E spatial distribution is more difficult, as they both differ from the statistical pictures in several respects, although GUMICS-5 results in our case have some similar features (Evening sector hot spot and heating in the polar cap) as in the empirical the model of Weimer (2005).

We recognize that GUMICS and the SWMF version that have been used in this study both have rather elementary approaches in their Pedersen conductance determination. More advanced ways are presented e.g. by Mukhopadhyay et al. (2022) and Lin et al. (2021). The most recent SWMF runs have been combined with the MAGNetosphere-Ionosphere-Thermosphere (MAGNIT) aurora model (Mukhopadhyay et al., 2022) which derives Pedersen conductance using four different sources of particle precipitation: diffuse ion and electron precipitation, monoenergetic electron precipitation and broadband electron precipitation. All these sources are derived from magnetospheric MHD parameters and their contributions are mutually balanced with loss-cone filling rates which are adjusted so that precipitation fluxes are statistically consistent with an extensive set of empirical models. Diffuse precipitation components (Σ_{pdi} and Σ_{pde}) and the monoenergetic component (Σ_{pm}) of conductance are linked with magnetospheric number density and temperature. Monoenergetic component depends also on the difference between magnetic fields at the magnetospheric plasma sheet and in the ionosphere. The broadband component is linked with the Poynting flux flowing into the ionosphere. Total conductance is computed as vector sum of diffuse precipitation and monoenergetic components ($\sqrt{\Sigma_{pdi}^2 + \Sigma_{pde}^2 + \Sigma_{pm}^2}$) and on top of that the contribution of the broadband component is added linearly. The broadband component is assumed to enhance conductance at the lower parts of ionospheric F-layer, which motivates its linear summing with the other components impacting E-layer. Mukhopadhyay et al. (2022) demonstrate MAGNIT performance with a simulation of a well documented geomagnetic storm. In their conductance results the joint contribution of diffuse and monoenergetic electron precipitations is ~40% of the total conductance. This suggests that besides the MHD results also our ASC-based Q_E results are under-estimates because 557.7 nm optical data give information only on electron monoenergetic and diffuse precipitation. The role of diffuse electron precipitation as a crucial conductance source is confirmed both by observations (Newell et al., 2009) and by modeling with the Multiscale Atmosphere Geospace Environment (MAGE) which combines MHD with ring current and thermospheric models (Lin et al., 2021).

Handling plasma populations in near-Earth space with velocity distribution functions – like done in the Vlasiator hybrid simulation (von Alfthan et al., 2014; Palmroth et al., 2018) – is a computationally demanding approach, but it offers the way to gain a more realistic picture on Joule Heating spatio-temporal variations with their background in magnetospheric processes. Observational validation of hybrid simulations' performance in Q_E characterization will be difficult on global scales, but on regional scales it will be possible, by combining ground-based and LEO satellite observations, like described in this study. Q_E estimates based on regional KRM analysis of ground-based ASC and magnetometer data can be validated by comparing their results on FAC and **E**-field with corresponding parameters from LEO satellite data. ESA Swarm satellites are particularly useful for this purpose as they provide thermospheric density estimates in addition to **B**- and **E**-field data. Our KRM-analysis of a stable evening sector arc system yields Q_E estimates of ~3.0 mW/m^2 located not at the arcs but in their vicinity region, where the electric field is enhanced but Pedersen conductance is low. These results are consistent with findings from earlier evening sector arc studies (Aikio et al., 2002). GUMICS-5 Q_E estimates for our case are smaller than the observed values by a factor of 2.88.

Estimation of Joule heating by a mix of Swarm and ground data, as demonstrated in this study by taking conductance estimates from ground data and **E**-field from Swarm provides a means to address weak events, like many of the auroral arcs observed under low activity conditions. In our particular case, consistency was shown to hold between different estimates of the same quantity (FAC, electric field). The average Joule heating on the regional scale based on observed data (1.4 mW/m^2) was found in a good agreement with the simulation results of maxima Q_E along the Swarm trajectory (~1.5 mW/m^2 for SWMF and ~1.25 mW/m^2 for GUMICS-5). Although there is a mismatch in the latitudinal location of enhanced Q_E by the simulations and the regional observations, the consistency in Q_E intensities can be regarded as a noteworthy result when considering the widely different underlying conditions and assumptions, as well as the diversity of tools and data used to derive Q_E estimates. Given the large number of conjunctions between Swarm and ground stations, consistency across scales can be explored for further events, by observations and simulations.

8. Conclusions and future prospects

Empirical models on global high latitude Q_E variations have been published in literature (Olsson et al., 2004; Weimer, 2005; Zhang

et al., 2005), but their results show larger variability among themselves than statistical models on large scale FACs, auroral precipitation, and polar plasma convection. Enhanced Joule Heating is known to drive increased thermospheric densities at typical LEO orbit altitudes. Getting more detailed picture on where and when such driving takes place would be useful information for satellite drag assessments. Magnetosphere-ionosphere-thermosphere simulations have potential to provide such information.

We have studied performance of two MHD simulations – GUMICS-5 and SWMF – in estimating Q_E with a test event of a moderate substorm. The comparison shows that differences between the two codes appear not just in the Q_E intensity, but also in its spatial distribution in the MLT-MLAT frame. The root cause for these differences is in the way how the MHD parameters in the magnetosphere are coupled with the Pedersen conductance in the ionosphere. The two MHD codes show systematically smaller Q_E values than the CTIPe simulation code addressing ionosphere-thermosphere interactions. This difference is mostly explained by the convection electric field of CTIPe which is enhanced by a randomly varying additional component mimicking small scale structures.

Our study includes also a regional analysis of Q_E estimates, where MHD results are compared with outputs by a regional KRM-analysis of ground-based (GB) auroral camera and magnetometer data and by an analysis which combines Pedersen conductance by KRM with Swarm satellite observations of electric field. The GB-KRM and Swarm approaches give mutually consistent results on the electric field and Q_E. GUMICS-5 estimate of Q_E in the test region (growth phase arc system in the evening sector) shows different latitude distribution than the GB-KRM result and its peak value is smaller than that from the ground-based data by a factor of 2.9. However, a rather good consistency was found between the average of Q_E by the Swarm approach as computed along the satellite track across the test area and the peak Q_E values by the MHD simulations (relative errors ~10%).

It is good to keep in mind that careful Joule Heating assessments cannot be made if the role of neutral wind, either as an inhibiting or as a catalyzing factor, is ignored. Under this theme several useful surveys have been done as part of the proposal work for the ESA Earth Explorer candidate mission Daedalus (Sarris et al., 2020; Palmroth et al., 2021). Although Daedalus was not selected for immediate continuation and further effort by an ESA-NASA working group is currently ongoing, its preparatory work has paved the way for future modeling and observations of thermospheric impacts on ionospheric electrodynamics. Significant contributions to this research area can be expected also when the forthcoming upgrading of the EISCAT ISR system, EISCAT_3D, will start operations. The new radars will provide by multiple simultaneous beams volumetric measurements from an altitude range (70–1500 km) that is crucial for ionosphere–thermosphere interaction studies but beyond the reach of satellite measurements in its lower parts where the critical collisional physics takes place (McCrea et al., 2015).

A key ingredient for both observations and simulations is conductance, which is difficult to derive with good accuracy, in particular at small values. At the same time, regions with low conductance are often the site of significant Q_E, because of the particular coupling regime between magnetosphere and ionosphere, with the magnetosphere acting as a current generator, rather than a voltage generator. Obviously, future estimates of the global energetics in the magnetosphere–ionosphere–thermosphere system require better conductance – and conductivity – data. While Swarm ability to make accurate conductance measurements is limited, as discussed also in this paper, significant progress could be achieved by a Daedalus-like mission, getting close enough to the ionospheric E-layer and providing systematic observation of the Joule heating and its ingredients, in particular conductivity. Coordination between a very low altitude mission, like Daedalus, and a topside ionospheric mission, like Swarm, could fully exploit the complementarity between height-resolved and height integrated observations, enhancing thus the return of both missions.

CRediT authorship contribution statement

Kirsti Kauristie: Conceptualization, Writing – original draft. **Octav Marghitu:** Conceptualization, Methodology, Writing – original draft. **Max van de Kamp:** Methodology, Software. **Theresa Hoppe:** Methodology, Software. **Ilja Honkonen:** Methodology, Software. **Adrian Blagau:** Methodology, Software. **Ionut Madalin Ivan:** Software. **Mihail Codrescu:** Supervision. **Aaron Ridley:** Supervision. **Gábor Tóth:** Supervision. **Yasunobu Ogawa:** Supervision. **Lorenzo Trenchi:** Conceptualization.

Declaration of competing interest

The authors declare that they have no known competing financial interests or personal relationships that could have appeared to influence the work reported in this paper.

Data availability

Data will be made available on request.

Acknowledgments

This work has been supported by the SIFACIT project, ESA contract 4000118383/16/I-EF. We thank the institutes who maintain the IMAGE Magnetometer Array (used in our KRM analysis): Tromsø Geophysical Observatory of UiT the Arctic University of Norway (Norway), Finnish Meteorological Institute (Finland), Institute of Geophysics Polish Academy of Sciences (Poland), GFZ German Research Centre for Geosciences (Germany), Geological Survey of Sweden (Sweden), Swedish Institute of Space Physics (Sweden), Sodankylä Geophysical Observatory of the University of Oulu (Finland), and DTU Technical University of Denmark (Denmark).

This work was carried out using the SWMF tools developed at the University of Michigan's Center for Space Environment Modeling (CSEM). The modeling tools described in this publication are available online through the University of Michigan for download and are available for use at the Community Coordinated Modeling Center (CCMC). The ccmc run id of the model used in this study is ilja_honkonen_012921_1.

World Data Center for Geomagnetism, Kyoto, is acknowledged for provision of the AE-indices.

References

Ahn, B.H., Akasofu, S.I., Kamide, Y., 1983. The joule heat production rate and the particle energy injection rate as function of the geomagnetic indices AE and AL. JGR 88 (A8), 6275–6287, URL http://onlinelibrary.wiley.com/doi/10.1029/JA088iA08p06275/pdf.

Aikio, A.T., Cai, L., Nygrén, T., 2012. Statistical distribution of height-integrated energy exchange rates in the ionosphere: Height-integrated energy transfer rates. J. Geophys. Res. Space Phys. 117 (A10), n/a–n/a. http://dx.doi.org/10.1029/2012JA018078, URL http://doi.wiley.com/10.1029/2012JA018078.

Aikio, A.T., Lakkala, T., Kozlovsky, A., Williams, P.J.S., 2002. Electric fields and currents of stable drifting auroral arcs in the evening sector. J. Geophys. Res. Space Phys. 107 (A12), SIA 3–1–SIA 3–14. http://dx.doi.org/10.1029/2001JA009172, URL http://doi.wiley.com/10.1029/2001JA009172.

Aikio, A.T., Selkälä, A., 2009. Statistical properties of Joule heating rate, electric field and conductances at high latitudes. Ann. Geophys. 27 (7), 2661–2673. http://dx.doi.org/10.5194/angeo-27-2661-2009, URL https://angeo.copernicus.org/articles/27/2661/2009/.

Amm, O., Vanhamäki, H., Kauristie, K., Stolle, C., Christiansen, F., Haagmans, R., Masson, A., Taylor, M.G.G.T., Floberghagen, R., Escoubet, C.P., 2015. A method to derive maps of ionospheric conductances, currents, and convection from the Swarm multisatellite mission. J. Geophys. Res. Space Phys. 120 (4), 3263–3282. http://dx.doi.org/10.1002/2014JA020154, URL http://doi.wiley.com/10.1002/2014JA020154.

Amm, O., Viljanen, A., 1999. Ionospheric disturbance magnetic field continuation from the ground to the ionosphere using spherical elementary current systems. Earth, Planets Space 51 (6), 431–440. http://dx.doi.org/10.1186/BF03352247, URL http://earth-planets-space.springeropen.com/articles/10.1186/BF03352247.

Blagau, A., Vogt, J., 2019. Multipoint Field-Aligned Current Estimates With Swarm. J. Geophys. Res. Space Phys. 124 (8), 6869–6895. http://dx.doi.org/10.1029/2018JA026439, URL https://onlinelibrary.wiley.com/doi/10.1029/2018JA026439.

Cai, L., Aikio, A.T., Milan, S.E., 2016. Joule heating hot spot at high latitudes in the afternoon sector: Afternoon Joule heating hot spot. J. Geophys. Res. Space Phys. 121 (7), 7135–7152. http://dx.doi.org/10.1002/2016JA022432, URL http://doi.wiley.com/10.1002/2016JA022432.

Chun, F.K., Knipp, D.J., McHarg, M.G., Lacey, J.R., Lu, G., Emery, B.A., 2002. Joule heating patterns as a function of polar cap index. J. Geophys. Res. 107 (A7), 1119. http://dx.doi.org/10.1029/2001JA000246, URL http://doi.wiley.com/10.1029/2001JA000246.

Chun, F., Knipp, D., McHarg, M., Lu, G., Emery, B., Vennerström, S., Troshichev, O.A., 1999. Polar cap index as a proxy for hemispheric Joule heating. GRL 26 (8), 1101–1104. http://dx.doi.org/10.1029/1999GL900196, URL http://doi.wiley.com/10.1029/1999GL900196.

Codrescu, M.V., Fuller-Rowell, T.J., Foster, J.C., 1995. On the importance of E-field variability for Joule heating in the high-latitude thermosphere. Geophys. Res. Lett. 22 (17), 2393–2396. http://dx.doi.org/10.1029/95GL01909, URL http://doi.wiley.com/10.1029/95GL01909.

Codrescu, M.V., Fuller-Rowell, T.J., Foster, J.C., Holt, J.M., Cariglia, S.J., 2000. Electric field variability associated with the millstone hill electric field model. J. Geophys. Res. Space Phys. 105 (A3), 5265–5273. http://dx.doi.org/10.1029/1999JA900463, URL http://doi.wiley.com/10.1029/1999JA900463.

Codrescu, M.V., Negrea, C.a.a., Fedrizzi, M., Fuller-Rowell, T.J., Dobin, A., Jakowsky, N., Khalsa, H., Matsuo, T., Maruyama, N., 2012. A real-time run of the coupled thermosphere ionosphere plasmasphere electrodynamics (CTIPe) model: A real-time run of the ctipe model. Space Weather 10 (2), n/a–n/a. http://dx.doi.org/10.1029/2011SW000736, URL http://doi.wiley.com/10.1029/2011SW000736.

Davis, T.N., Sugiura, M., 1966. Auroral electrojet activity index AE and its universal time variations. J. Geophys. Res. 71 (3), 785–801. http://dx.doi.org/10.1029/jz071i003p00785.

Elphic, R.C., Bonnell, J.W., Strangeway, R.J., Kepko, L., Ergun, R.E., McFadden, J.P., Carlson, C.W., Peria, W., Cattell, C.A., Klumpar, D., Shelley, E., Peterson, W., Moebius, E., Kistler, L., Pfaff, R., 1998. The auroral current circuit and field-aligned currents observed by FAST. Geophys. Res. Lett. 25 (12), 2033–2036. http://dx.doi.org/10.1029/98GL01158, URL http://doi.wiley.com/10.1029/98GL01158.

Evans, D.S., Maynard, N.C., Trøim, J., Jacobsen, T., Egeland, A., 1977. Auroral vector electric field and particle comparisons, 2, Electrodynamics of an arc. J. Geophys. Res. 82 (16), 2235–2249. http://dx.doi.org/10.1029/JA082i016p02235, URL http://doi.wiley.com/10.1029/JA082i016p02235.

Friis-Christensen, E., Lühr, H., Hulot, G., 2006. Swarm: A constellation to study the Earth's magnetic field. EPS 58 (4), 351–358.

Gombosi, T.I., Dezeeuw, D.L., Groth, C.P.T., Powell, K.G., Clauer, R.C., Song, P., 2013. From Sun to Earth: Multiscale MHD simulations of space weather. In: Song, P., Singer, H.J., Siscoe, G.L. (Eds.), Geophysical Monograph Series. American Geophysical Union, Washington, D. C., pp. 169–176. http://dx.doi.org/10.1029/GM125p0169, URL http://doi.wiley.com/10.1029/GM125p0169.

Hedin, A.E., 1991. Extension of the MSIS thermosphere model into the middle and lower atmosphere. J. Geophys. Res. Space Phys. 96 (A2), 1159–1172. http://dx.doi.org/10.1029/90JA02125, URL http://doi.wiley.com/10.1029/90JA02125.

Honkonen, I., van de Kamp, M., Hoppe, T., Kauristie, K., 2022. Over 20-year global magnetohydrodynamic simulation of Earth's magnetosphere. Space Weather 20 (11), http://dx.doi.org/10.1029/2022SW003196, URL https://onlinelibrary.wiley.com/doi/10.1029/2022SW003196.

Janhunen, P., Palmroth, M., Laitinen, T., Honkonen, I., Juusola, L., Facskó, G., Pulkkinen, T., 2012. The GUMICS-4 global MHD magnetosphere–ionosphere coupling simulation. J. Atmos. Sol.-Terr. Phys. 80, 48–59. http://dx.doi.org/10.1016/j.jastp.2012.03.006, URL https://linkinghub.elsevier.com/retrieve/pii/S1364682612000909.

Juusola, L., Archer, W.E., Kauristie, K., Burchill, J.K., Vanhamäki, H., Aikio, A.T., 2016. Ionospheric conductances and currents of a morning sector auroral arc from Swarm-A electric and magnetic field measurements. Geophys. Res. Lett. 43 (22), http://dx.doi.org/10.1002/2016GL070248, URL https://agupubs.onlinelibrary.wiley.com/doi/10.1002/2016GL070248.

Kavanagh, A.J., Ogawa, Y., Woodfield, E.E., 2022. Two techniques for determining F-region ion velocities at meso-scales: Differences and impacts on Joule heating. J. Geophys. Res. Space Phys. 127 (6), http://dx.doi.org/10.1029/2021JA030062, URL https://onlinelibrary.wiley.com/doi/10.1029/2021JA030062.

Knudsen, D.J., Burchill, J.K., Buchert, S.C., Eriksson, A.I., Gill, R., Wahlund, J.E., Åhlen, L., Smith, M., Moffat, B., 2017. Thermal ion imagers and Langmuir probes in the Swarm electric field instruments. J. Geophys. Res. Space Phys. 122 (2), 2655–2673. http://dx.doi.org/10.1002/2016JA022571, URL https://onlinelibrary.wiley.com/doi/abs/10.1002/2016JA022571.

Lin, D., Sorathia, K., Wang, W., Merkin, V., Bao, S., Pham, K., Wiltberger, M., Shi, X., Toffoletto, F., Michael, A., Lyon, J., Garretson, J., Anderson, B., 2021. The role of diffuse electron precipitation in the formation of subauroral polarization streams. J. Geophys. Res. Space Phys. 126 (12), http://dx.doi.org/10.1029/2021JA029792, URL https://onlinelibrary.wiley.com/doi/10.1029/2021JA029792.

Loto'aniu, P.T.M., Romich, K., Rowland, W., Codrescu, S., Biesecker, D., Johnson, J., Singer, H.J., Szabo, A., Stevens, M., 2022. Validation of the DSCOVR spacecraft mission space weather solar wind products. Space Weather 20 (10), http://dx.doi.org/10.1029/2022SW003085, URL https://onlinelibrary.wiley.com/doi/10.1029/2022SW003085.

Lysak, R.L., 1985. Auroral electrodynamics with current and voltage generators. J. Geophys. Res. 90 (A5), 4178. http://dx.doi.org/10.1029/JA090iA05p04178, URL http://doi.wiley.com/10.1029/JA090iA05p04178.

McCrea, I., Aikio, A., Alfonsi, L., Belova, E., Buchert, S., Clilverd, M., Engler, N., Gustavsson, B., Heinselman, C., Kero, J., Kosch, M., Lamy, H., Leyser, T., Ogawa, Y., Oksavik, K., Pellinen-Wannberg, A., Pitout, F., Rapp, M., Stanislawska, I., Vierinen, J., 2015. The science case for the EISCAT_3D radar. Prog. Earth Planet. Sci. 2 (1), 21. http://dx.doi.org/10.1186/s40645-015-0051-8, URL http://www.progearthplanetsci.com/content/2/1/21.

Moen, J., Brekke, A., 1993. The solar flux influence on quiet time conductances in the auroral ionosphere. Geophys. Res. Lett. 20 (10), 971–974. http://dx.doi.org/10.1029/92GL02109, URL http://doi.wiley.com/10.1029/92GL02109.

Mukhopadhyay, A., Welling, D., Liemohn, M., Ridley, A., Burleigh, M., Wu, C., Zou, S., Connor, H., Vandegriff, E., Dredger, P., Tóth, G., 2022. Global driving of auroral precipitation: 1. balance of sources. J. Geophys. Res. Space Phys. 127 (7), http://dx.doi.org/10.1029/2022JA030323, URL https://onlinelibrary.wiley.com/doi/10.1029/2022JA030323.

Newell, P.T., Sotirelis, T., Wing, S., 2009. Diffuse, monoenergetic, and broadband aurora: The global precipitation budget: Global precipitation budget. J. Geophys. Res. Space Phys. 114 (A9), n/a–n/a. http://dx.doi.org/10.1029/2009JA014326, URL http://doi.wiley.com/10.1029/2009JA014326.

Olsson, A., Janhunen, P., Karlsson, T., Ivchenko, N., Blomberg, L.G., 2004. Statistics of Joule heating in the auroral zone and polar cap using Astrid-2 satellite poynting flux. Ann. Geophys. 22 (12), 4133–4142. http://dx.doi.org/10.5194/angeo-22-4133-2004, URL https://angeo.copernicus.org/articles/22/4133/2004/.

Palmroth, M., Ganse, U., Pfau-Kempf, Y., Battarbee, M., Turc, L., Brito, T., Grandin, M., Hoilijoki, S., Sandroos, A., von Alfthan, S., 2018. Vlasov methods in space physics and astrophysics. Living Rev. Comput. Astrophys. 4 (1), 1. http://dx.doi.org/10.1007/s41115-018-0003-2, URL http://link.springer.com/10.1007/s41115-018-0003-2.

Palmroth, M., Grandin, M., Sarris, T., Doornbos, E., Tourgaidis, S., Aikio, A., Buchert, S., Clilverd, M.A., Dandouras, I., Heelis, R., Hoffmann, A., Ivchenko, N., Kervalishvili, G., Knudsen, D.J., Kotova, A., Liu, H.-L., Malaspina, D.M., March, G., Marchaudon, A., Marghitu, O., Matsuo, T., Miloch, W.J., Moretto-Jørgensen, T., Mpaloukidis, D., Olsen, N., Papadakis, K., Pfaff, R., Pirnaris, P., Siemes, C., Stolle, C., Suni, J., van den IJssel, J., Verronen, P.T., Visser, P., Yamauchi, M., 2021. Lower-thermosphere–ionosphere (LTI) quantities: current status of measuring techniques and models. Ann. Geophys. 39 (1), 189–237. http://dx.doi.org/10.5194/angeo-39-189-2021, URL https://angeo.copernicus.org/articles/39/189/2021/.

Palmroth, M., Janhunen, P., Pulkkinen, T.I., Aksnes, A., Lu, G., Østgaard, N., Watermann, J., Reeves, G.D., Germany, G.A., 2005. Assessment of ionospheric Joule heating by GUMICS-4 MHD simulation, AMIE, and satellite-based statistics: towards a synthesis. Ann. Geophys. 23 (6), 2051–2068. http://dx.doi.org/10.5194/angeo-23-2051-2005, URL https://angeo.copernicus.org/articles/23/2051/2005/.

Partamies, N., Janhunen, P., Kauristie, K., Mäkinen, S., Sergienko, T., 2004. Testing an inversion method for estimating electron energy fluxes from all-sky camera images. Ann. Geophys. 22 (6), 1961–1971. http://dx.doi.org/10.5194/angeo-22-1961-2004, URL https://angeo.copernicus.org/articles/22/1961/2004/.

Powell, K.G., Roe, P.L., Linde, T.J., Gombosi, T.I., De Zeeuw, D.L., 1999. A solution-adaptive upwind scheme for ideal magnetohydrodynamics. J. Comput. Phys. 154 (2), 284–309. http://dx.doi.org/10.1006/jcph.1999.6299, URL https://linkinghub.elsevier.com/retrieve/pii/S002199919996299X.

Rastätter, L., Shim, J.S., Kuznetsova, M.M., Kilcommons, L.M., Knipp, D.J., Codrescu, M., Fuller-Rowell, T., Emery, B., Weimer, D.R., Cosgrove, R., Wiltberger, M., Raeder, J., Li, W., Tóth, G., Welling, D., 2016. GEM-CEDAR challenge: Poynting flux at DMSP and modeled Joule heat. Space Weather 14 (2), 113–135. http://dx.doi.org/10.1002/2015SW001238, URL https://onlinelibrary.wiley.com/doi/10.1002/2015SW001238.

Richmond, A., 1992. Assimilative mapping of ionospheric electrodynamics. Adv. Space Res. 12 (6), 59–68. http://dx.doi.org/10.1016/0273-1177(92)90040-5, URL https://linkinghub.elsevier.com/retrieve/pii/0273117792900405.

Richmond, A., 2021. Joule heating in the thermosphere. In: Wang, W., Zhang, Y., Paxton, L. (Eds.), Upper Atmosphere Dynamics and Energetics, Geophysical Monograph Series 261. American Geophysical Union, pp. 1–18.

Richmond, A.D., Kamide, Y., 1988. Mapping electrodynamic features of the high-latitude ionosphere from localized observations: Technique. J. Geophys. Res. 93 (A6), 5741. http://dx.doi.org/10.1029/JA093iA06p05741, URL http://doi.wiley.com/10.1029/JA093iA06p05741.

Ridley, A.J., Gombosi, T.I., DeZeeuw, D.L., 2004. Ionospheric control of the magnetosphere: conductance. Ann. Geophys. 22 (2), 567–584. http://dx.doi.org/10.5194/angeo-22-567-2004, URL https://angeo.copernicus.org/articles/22/567/2004/.

Ritter, P., Lühr, H., Rauberg, J., 2013. Determining field-aligned currents with the Swarm constellation mission. Earth, Planets Space 65 (11), 1285–1294. http://dx.doi.org/10.5047/eps.2013.09.006, URL http://link.springer.com/10.5047/eps.2013.09.006.

Robinson, R.M., Vondrak, R.R., Miller, K., Dabbs, T., Hardy, D., 1987. On calculating ionospheric conductances from the flux and energy of precipitating electrons. J. Geophys. Res. 92 (A3), 2565. http://dx.doi.org/10.1029/JA092iA03p02565, URL http://doi.wiley.com/10.1029/JA092iA03p02565.

Sangalli, L., Knudsen, D.J., Larsen, M.F., Zhan, T., Pfaff, R.F., Rowland, D., 2009. Rocket-based measurements of ion velocity, neutral wind, and electric field in the collisional transition region of the auroral ionosphere: E Region ion demagnetization. J. Geophys. Res. Space Phys. 114 (A4), n/a–n/a. http://dx.doi.org/10.1029/2008JA013757, URL http://doi.wiley.com/10.1029/2008JA013757.

Sangalli, L., Partamies, N., Syrjäsuo, M., Enell, C.F., Kauristie, K., Mäkinen, S., 2011. Performance study of the new EMCCD-based all-sky cameras for auroral imaging. Int. J. Remote Sens. 32 (11), 2987–3003. http://dx.doi.org/10.1080/01431161.2010.541505, URL https://www.tandfonline.com/doi/full/10.1080/01431161.2010.541505.

Sarris, T.E., Talaat, E.R., Palmroth, M., Dandouras, I., Armandillo, E., Kervalishvili, G., Buchert, S., Tourgaidis, S., Malaspina, D.M., Jaynes, A.N., Paschalidis, N., Sample, J., Halekas, J., Doornbos, E., Lappas, V., Moretto Jørgensen, T., Stolle, C., Clilverd, M., Wu, Q., Sandberg, I., Pirnaris, P., Aikio, A., 2020. Daedalus: A low-flying spacecraft for in situ exploration of the lower thermosphere–ionosphere. Geosci. Instrum., Methods Data Syst. 9 (1), 153–191. http://dx.doi.org/10.5194/gi-9-153-2020, URL https://gi.copernicus.org/articles/9/153/2020/.

Tanskanen, E., 2002. Substorm energy budget during low and high solar activity: 1997 and 1999 compared. J. Geophys. Res. 107 (A6), 1086. http://dx.doi.org/10.1029/2001JA900153, URL http://doi.wiley.com/10.1029/2001JA900153.

Tanskanen, E.I., 2009. A comprehensive high-throughput analysis of substorms observed by IMAGE magnetometer network: Years 1993–2003 examined. JGR 114, A05204. http://dx.doi.org/10.1029/2008JA013682, URL http://onlinelibrary.wiley.com/doi/10.1029/2008JA013682/full.

Tøffner-Clausen, L., Lesur, V., Olsen, N., Finlay, C.C., 2016. In-flight scalar calibration and characterisation of the Swarm magnetometry package. Earth, Planets Space 68 (1), 129. http://dx.doi.org/10.1186/s40623-016-0501-6, URL http://earth-planets-space.springeropen.com/articles/10.1186/s40623-016-0501-6.

Tóth, G., Sokolov, I.V., Gombosi, T.I., Chesney, D.R., Clauer, C.R., De Zeeuw, D.L., Hansen, K.C., Kane, K.J., Manchester, W.B., Oehmke, R.C., Powell, K.G., Ridley, A.J., Roussev, I.I., Stout, Q.F., Volberg, O., Wolf, R.A., Sazykin, S., Chan, A., Yu, B., Kóta, J., 2005. Space weather modeling framework: A new tool for the space science community. J. Geophys. Res. 110 (A12), A12226. http://dx.doi.org/10.1029/2005JA011126, URL http://doi.wiley.com/10.1029/2005JA011126.

Tóth, G., Van Der Holst, B., Sokolov, I.V., De Zeeuw, D.L., Gombosi, T.I., Fang, F., Manchester, W.B., Meng, X., Najib, D., Powell, K.G., Stout, Q.F., Glocer, A., Ma, Y.J., Opher, M., 2012. Adaptive numerical algorithms in space weather modeling. J. Comput. Phys. 231 (3), 870–903. http://dx.doi.org/10.1016/j.jcp.2011.02.006, URL https://linkinghub.elsevier.com/retrieve/pii/S002199911100088X.

Troshichev, O., Andrezen, V., Vennerström, S., Friis-Christensen, E., 1988. Magnetic activity in the polar cap - A new index. PSS 36 (11), 1095–1102. http://dx.doi.org/10.1016/0032-0633(88)90063-3.

Vanhamäki, H., Amm, O., 2007. A new method to estimate ionospheric electric fields and currents using data from a local ground magnetometer network. Ann. Geophys. 25 (5), 1141–1156. http://dx.doi.org/10.5194/angeo-25-1141-2007, URL https://angeo.copernicus.org/articles/25/1141/2007/.

Vanhamäki, H., Kauristie, K., Amm, O., Senior, A., Lummerzheim, D., Milan, S., 2009. Electrodynamics of an omega-band as deduced from optical and magnetometer data. Ann. Geophys. 27 (9), 3367–3385. http://dx.doi.org/10.5194/angeo-27-3367-2009, URL https://angeo.copernicus.org/articles/27/3367/2009/.

Vanhamäki, H., Yoshikawa, A., Amm, O., Fujii, R., 2012. Ionospheric Joule heating and poynting flux in quasi-static approximation: Joule heating and poynting flux. J. Geophys. Res. Space Phys. 117 (A8), n/a–n/a. http://dx.doi.org/10.1029/2012JA017841, URL http://doi.wiley.com/10.1029/2012JA017841.

Vogt, J., Haerendel, G., Glassmeier, K.H., 1999. A model for the reflection of Alfvén waves at the source region of the Birkeland current system: The Tau generator. J. Geophys. Res. Space Phys. 104 (A1), 269–278. http://dx.doi.org/10.1029/1998JA900048, URL http://doi.wiley.com/10.1029/1998JA900048.

Vogt, J., Sorbalo, E., He, M., Blagau, A., 2013. Gradient estimation using configurations of two or three spacecraft. Ann. Geophys. 31 (11), 1913–1927. http://dx.doi.org/10.5194/angeo-31-1913-2013, URL https://angeo.copernicus.org/articles/31/1913/2013/.

von Alfthan, S., Pokhotelov, D., Kempf, Y., Hoilijoki, S., Honkonen, I., Sandroos, A., Palmroth, M., 2014. Vlasiator: First global hybrid-Vlasov simulations of Earth's foreshock and magnetosheath. J. Atmos. Sol.-Terr. Phys. 120, 24–35. http://dx.doi.org/10.1016/j.jastp.2014.08.012, URL https://linkinghub.elsevier.com/retrieve/pii/S1364682614001916.

Weimer, D.R., 2005. Improved ionospheric electrodynamic models and application to calculating Joule heating rates. J. Geophys. Res. 110 (A5), A05306. http://dx.doi.org/10.1029/2004JA010884, URL http://doi.wiley.com/10.1029/2004JA010884.

Zhan, W., Kaeppler, S.R., Larsen, M.F., Reimer, A., Varney, R., 2021. An investigation of auroral E region energy exchange using Poker Flat incoherent scatter radar observations during fall equinox conditions. J. Geophys. Res. Space Phys. 126 (10), http://dx.doi.org/10.1029/2021JA029371, URL https://onlinelibrary.wiley.com/doi/10.1029/2021JA029371.

Zhang, X.X., Wang, C., Chen, T., Wang, Y.L., Tan, A., Wu, T.S., Germany, G.A., Wang, W., 2005. Global patterns of Joule heating in the high-latitude ionosphere. J. Geophys. Res. 110 (A12), A12208. http://dx.doi.org/10.1029/2005JA011222, URL http://doi.wiley.com/10.1029/2005JA011222.

Zwickl, R.D., Doggett, K.A., Sahm, S., Barrett, W.P., Grubb, R.N., Detman, T.R., Raben, V.J., Smith, C.W., Riley, P., Gold, R.E., Mewaldt, R.A., Maruyama, T., 1998. The NOAA real-time solar-wind (RTSW) system using ACE data. In: Russell, C.T., Mewaldt, R.A., Von Rosenvinge, T.T. (Eds.), The Advanced Composition Explorer Mission. Springer Netherlands, Dordrecht, pp. 633–648. http://dx.doi.org/10.1007/978-94-011-4762-0_22, URL http://link.springer.com/10.1007/978-94-011-4762-0_22.